



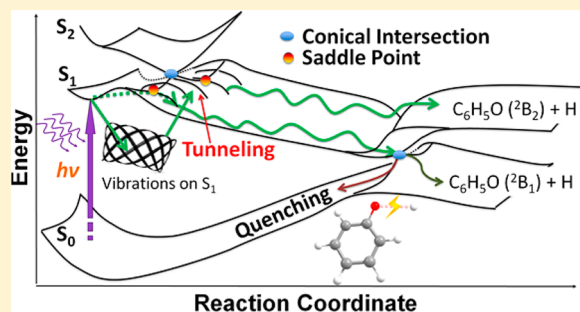
Photodissociation Dynamics of Phenol: Multistate Trajectory Simulations including Tunneling

Xuefei Xu, Jingjing Zheng, Ke R. Yang, and Donald G. Truhlar*

Department of Chemistry, Chemical Theory Center, and Supercomputing Institute, University of Minnesota, Minneapolis, Minnesota 55455-0431, United States

Supporting Information

ABSTRACT: We report multistate trajectory simulations, including coherence, decoherence, and multidimensional tunneling, of phenol photodissociation dynamics. The calculations are based on full-dimensional anchor-points reactive potential surfaces and state couplings fit to electronic structure calculations including dynamical correlation with an augmented correlation-consistent polarized valence double- ζ basis set. The calculations successfully reproduce the experimentally observed bimodal character of the total kinetic energy release spectra and confirm the interpretation of the most recent experiments that the photodissociation process is dominated by tunneling. Analysis of the trajectories uncovers an unexpected dissociation pathway for one quantum excitation of the O–H stretching mode of the S_1 state, namely, tunneling in a coherent mixture of states starting in a smaller R_{OH} (~ 0.9 – 1.0 Å) region than has previously been invoked. The simulations also show that most trajectories do not pass close to the S_1 – S_2 conical intersection (they have a minimum gap greater than 0.6 eV), they provide statistics on the out-of-plane angles at the locations of the minimum energy adiabatic gap, and they reveal information about which vibrational modes are most highly activated in the products.



INTRODUCTION

A natural protection mechanism of the fundamental building blocks of life, namely, the photostability of nucleic acid bases and amino acids against UV irradiation, is the existence of ultrafast nonradiative decay routes, such as ultrafast internal conversion (IC) of the UV-excited $^1\pi\pi^*$ state to the ground state.^{1–3} In phenol, a prototype molecule of the amino acid tyrosine, the main radiationless deactivation pathway under UV light is O–H bond fission to form H atom and phenoxyl radical; this process is driven by the dark $^1\pi\sigma^*$ state. In the past 10 years, the photodissociation dynamics of phenol and substituted phenols have been intensely investigated by both experimental and theoretical workers.^{4–19}

Figure 1 shows how the potential energy surfaces (PESs) evolve as the O–H stretch coordinate increases. The PES of the dark repulsive $^1\pi\sigma^*$ state (S_2 in Franck–Condon region) of phenol undergoes two conical intersections (CIs) with other PESs, first with the strongly absorbing bound $^1\pi\pi^*$ state (S_1), then with the ground $^1\pi\pi$ state (S_0). The two CIs play key roles in the photodissociation dynamics; their energetics and shapes determine the reaction mechanism and the branching ratios of photodissociation products for various UV wavelengths (λ). The most direct experimental observable is the relative kinetic energy distribution of photofragments, and that is found to be bimodal for excitation in the range $279.145 \geq \lambda \geq 193$ nm, as determined by a variety of techniques, including multimass ion imaging, high-resolution H Rydberg atom translational spec-

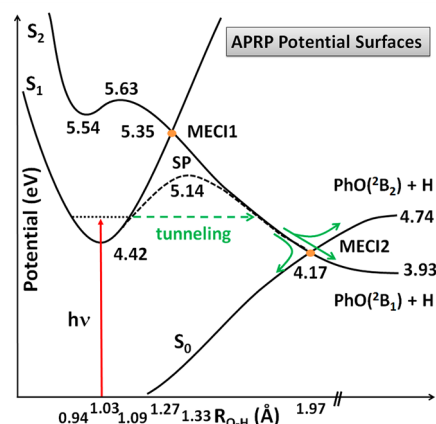


Figure 1. Schematic profiles of the APRP adiabatic potential energy surfaces used for the dynamics calculations of the photodissociation of phenol. MECI denotes the minimum energy point on a conical intersection seam, and SP denotes a saddle point. Energies (in eV) of MECIs, SPs, and asymptotes are given in the figure. The zero of energy is the minimum of the S_0 state, which is not shown in the figure.

troscopy, and time-resolved velocity map ion imaging.^{5,7,8,10,13,14,16,17} The fast kinetic energy component shows

Received: September 1, 2014

Published: October 27, 2014



clear vibrational structures with a maximum at $\sim 6000\text{ cm}^{-1}$ for the 0–0 excitation ($\lambda = 275.113\text{ nm}$, $h\nu = 4.51\text{ eV}$); for $\lambda < 248\text{ nm}$ ($h\nu > 5.00\text{ eV}$), this peak gradually declines in intensity as λ is reduced, and a new structured peak grows in a region close to $\sim 12\,000\text{ cm}^{-1}$.^{7,8,16} The maximum of this new “faster” peak remains at $\sim 12\,000\text{ cm}^{-1}$, but the structure gradually disappears as λ is further reduced. The vibrationally unresolved slow component of the kinetic energy spectra is less sensitive to the UV wavelength and peaks at $\sim 1500\text{--}2000\text{ cm}^{-1}$.^{8,13,16}

On the basis of these observations, it was concluded that ground-electronic-state ($^2\text{B}_1$) phenoxyl radical (PhO) is the main product for various λ ; the slow kinetic energy component was explained as due to multiphoton processes⁴ or to the formation of H atoms and $^2\text{B}_1$ phenoxyl radicals via statistical decay⁸ of the S_0 state of phenol following IC. The first CI (CI1, $^1\pi\pi^*/^1\pi\sigma^*$) was estimated to have an energy of $\sim 5\text{ eV}$, and the fast kinetic energy centered at $\sim 12\,000\text{ cm}^{-1}$ for $\lambda < 248\text{ nm}$ was attributed to the ultrafast dissociation via the $^1\pi\sigma^*$ state after passing through this CI.⁷ The fast kinetic energy component peaking at $\sim 6000\text{--}6500\text{ cm}^{-1}$ for $\lambda > 248\text{ nm}$ has been explained by two mechanisms: one is IC to vibrationally excited states of the S_0 state of phenol with the OH stretch as the main accepting mode, then dissociation via the second CI (CI2, $^1\pi\pi^*/^1\pi\sigma^*$); another is via H tunneling through the barrier of the CI1 to the $^1\pi\sigma^*$ state.⁷ The latter mechanism is supported by the most recent investigations.^{15–17}

The fast-kinetic energy edge of the experimental kinetic energy distribution showed state-resolved excitations of specific vibrational modes of the $^2\text{B}_1$ phenoxyl radical product. These active modes, especially the most prominent excited mode, which is ν_{16a} , were interpreted as promoting the coupling between the $^1\pi\pi^*$ and $^1\pi\sigma^*$ states, thereby lowering the energy of S_1 state, and making the system more adiabatic and making it easier to tunnel through the barrier on the S_1 state for dissociation under long- λ irradiation.^{16,20}

The important insights from these previous studies whet one's appetite to understand the process more deeply. However, full dynamical simulations have been unavailable since they require including both electronic nonadiabaticity and tunneling for a system with 33 internal degrees of freedom, which has been beyond state-of-the-art capabilities. Our recent work showing how to include tunneling in classical²¹ and multistate²² simulations by the army ants algorithm is here combined with the coherent switches with decay-of-mixing algorithm (CSDM)²³ and coupled potential surfaces represented by the anchor-points reactive potential (APRP) method^{20,24} to allow full-dimensional simulations of the photodissociation dynamics of phenol.

METHODS

The present work is based on combining (for the first time) four theoretical methods for application to a single problem. The methods are the 4-fold way for diabaticization, the anchor-points reactive potential method for analytic representation of potential energy, the army ants semiclassical approximation for adding tunneling to molecular dynamics simulations, and the coherent switches with decay of mixing method for electronically nonadiabatic trajectory calculations. Although all four methods have been described in previous publications, we review them here as background to the presentation of the results of applying them to the photodissociation of phenol.

The 4-fold Way. Electronic structure calculations of the three lowest singlet states of phenol were carried out by multiconfiguration quasidegenerate perturbation theory²⁵ with the jul-cc-pVDZ basis set²⁶

and 12 active electrons in 11 active orbitals.¹⁹ Multiconfiguration quasidegenerate perturbation theory involves a complete active space self-consistent field calculation that provides reference functions for a model space electronic Hamiltonian constructed by second-order van Vleck perturbation theory; diagonalization of this effective electronic Hamiltonian provides the adiabatic potential surfaces including the effects of both static and dynamic electron correlation. The adiabatic surfaces are labeled V_1 , V_2 , and V_3 , in order of increasing energy; these 33-dimensional surfaces involve 31-dimensional conical intersection seams, where they intersect at cuspidal ridges, and the nonadiabatic coupling vectors that couple them become singular at these ridges. To make it affordable to perform lengthy trajectory calculations for large ensembles of initial conditions, we needed to fit the potential energy surfaces and couplings to analytic functions. To make this practical, we transformed to a diabatic basis. We define diabatic representations as those in which the surfaces are smooth, the dominant couplings are nonsingular smooth scalars, and the vector couplings can be assumed negligible.²⁷ The transformation was accomplished by the 4-fold way,²⁸ as explained elsewhere.¹⁹ The 4-fold way is a direct diabaticization method based on configurational uniformity. The diabatic potential energy surfaces are distinguished by their dominant configurations and are labeled U_1 ($^1\pi\pi$), U_2 ($^1\pi\pi^*$), and U_3 ($^1\pi\sigma^*$). Near the equilibrium geometry of phenol, V_i equals U_j ; between the first conical intersection (CI1) and the second conical intersection (CI2), we have $V_1 = U_1$, $V_2 = U_3$, and $V_3 = U_2$; and beyond the second conical intersection, we have $V_1 = U_3$, $V_2 = U_1$, and $V_3 = U_2$. Near the equilibrium geometry, the adiabatic states are also called S_0 , S_1 , and S_2 , but these labels can become ambiguous away from the equilibrium geometry.

The APRP Method. The anchor-points reactive potential method²⁴ is a recently developed PES fitting method applicable to moderate or large systems. It combines general analytic forms for large-amplitude modes with molecule-specific and anchor-point-specific molecular mechanics terms for small-amplitude modes to obtain full-dimensional semiglobal PESs. In our recent work,²⁰ the APRP method was used successfully to fit the above described diabatic potential energy surfaces and their couplings for photodissociation of phenol as functions of 33 nonredundant internal coordinates. We use these fits in the present simulations.

CSDM Method. The coherent switches with decay of mixing algorithm is a multistate semiclassical trajectory method, presented and explained elsewhere²³ and briefly summarized here. In CSDM, each trajectory is governed by a trajectory-specific Ehrenfest self-consistent potential (SCP), which is a weighted average of the potential energy surfaces, and which may also be called a mean-field potential or an effective potential V_{eff} . This effective potential corresponds to a coherent superpositions of states, and the method also includes decoherence that produces pure quantized final electronic states outside regions of strong coupling. The populations and coherences of the electronic states are defined in the usual way in terms of the electronic density matrix;²³ in particular the diagonal elements ρ_{jj} (which satisfy $0 \leq \rho_{jj} \leq 1$) are the instantaneous probabilities of being in each electronic state j ,²⁹ and they are the weights that determine the mean-field V_{eff} .

Army Ants Tunneling Algorithm. This is a quantum mechanical rare-event sampling algorithm for including multidimensional tunneling in molecular dynamics simulations.^{21,22} We assume that the electronic states are fully coherent in the tunneling region by using the SCP potential of the CSDM method but without decoherence; that is, decoherence is only included in classically allowed regions, but the elements of the electronic density matrix are allowed to change coherently during the tunneling event.

CALCULATIONS

Representation. In the present work, we propagate the trajectories in the adiabatic representation, for which the surfaces and their gradients and nonadiabatic vector couplings are obtained, as explained elsewhere,²³ at every time step by diagonalization of the fitted diabatic surfaces.

Initial Conditions. Simulations were carried out for three sets of initial conditions beginning in the S_1 state: one (labeled *a*) corresponding to the 0–0 excitation of $S_0 \rightarrow S_1$ and the other two (*b* and *c*) involving excitation of one quantum in ν_{OH} . Because classical trajectories redistribute vibrational energies unphysically if high-frequency modes are initialized with zero point energy (ZPE), our initial conditions are a combination of only slightly excited modes, classical modes, and quasiclassical modes, where “quasiclassical” is used in the sense common in the collision theory literature³⁰ to denote initial conditions that are classical except for having quantized vibration energies. The procedure of only slightly initially exciting some of the modes is similar to the constraint of freezing many modes,³¹ which is popular in biochemical simulations. For large molecules (like phenol or biological molecules), putting thermal or zero point energy in all modes would place a very large amount of energy in the whole system, but since that energy would be largely conserved by zero point constraints in a quantum mechanical system, but is not conserved in a highly excited anharmonic classical systems, the classical mechanics is expected to mimic the quantum mechanics better if most spectator modes have only small vibrational excitation. Employing a small amount of vibrational energy and allowing the mode to be flexible and to accept energy if provided dynamically is, however, expected to be a better model than completely freezing the vibrational modes, and that is adopted here for some of the modes. The prepared initial conditions for trajectories correspond to experiments that use long pump pulses to populate a narrow band of vibrational levels of the S_1 state, but they do not correspond precisely to any particular experiment (it is hard to precisely simulate experimental initial conditions in trajectory calculations due to the classical nature of the vibrations in such calculations). Nevertheless, we can say that in an approximate way, ensemble *a* approximately simulates the experimental 0–0 excitation, and ensembles *b* and *c* simulate excitation of one quantum of the ν_{OH} mode in the S_1 state with the energy in other vibrational modes being very low (case *b*) or low (case *c*). To ensure that the dissociative events we observe occur before significant unphysical vibrational energy redistribution, we run many 10 ps trajectories rather than a smaller number of long trajectories. The specific initial vibrational energy in each mode is provided in the next paragraph.

The 10 out-of-plane vibrational modes, which can promote the diabatic couplings, are initialized with a vibrational energy that is the maximum of ZPE of that mode or 0.013 eV (the classical average thermal mode energy at a vibrational temperature of 150 K, which we assume here to be typical of possible experimental conditions). The in-plane modes except ν_{OH} are given a very small vibrational energy of 0.001 eV for cases *a* and *b* and 0.013 eV for case *c*; the ν_{OH} mode is initialized with vibrational quantum number $n = 0$ (ZPE) in case *a* and $n = 1$ in the other two cases.

Initial conditions *a*, *b*, and *c* have total energies E of 4.94, 5.35, and 5.61 eV, respectively. Table 1 gives the energies for each case to reach MECI1 (the minimum energy point on the first conical intersection seam), the S_1 saddle point (SP), or each electronic state of the product if the vibrational energies of bound vibrational modes were conserved. These energetics are also indicated in Figure 2. The energies given in Figure 2 and Table 1 are the sums of the potential energy and vibrational energy terms at each stationary point, and the clearest way to explain their usage for interpretation purposes is with an example. Take ensemble *a* in Figure 2 as an example; the initial

Table 1. Summary of the Trajectory Simulations

| total energy E (eV) | (a) 4.94 | (b) 5.35 | (c) 5.61 |
|--|----------|----------|----------|
| MECI1 ^a | 5.66 eV | 5.66 eV | 5.93 eV |
| SP ^a | 5.45 eV | 5.45 eV | 5.72 eV |
| Excited 2B_2 state of phenoxyl + H ^b | 5.04 eV | 5.04 eV | 5.29 eV |
| Ground state of phenoxyl + H ^b | 4.23 eV | 4.23 eV | 4.48 eV |
| Total number of trajectories | 117181 | 25597 | 34009 |
| Number of reactive trajectories | 560 | 7631 | 10362 |
| Number of reactive trajectories without tunneling | 0 | 1 | 8 |
| $\langle t \rangle$ (fs) ^c | 384 | 871 | 276 |

^aThis row gives the energy that would be needed to reach this point if all vibrational energies except the O–H stretch mode were conserved. Although these vibrational energies are not conserved, the energetic requirement for the process if they were conserved provides a useful guide to understanding the energetics of the trajectories. ^bThis row gives the energy that would be needed to reach this point if vibrational energies of all modes except those that disappear upon dissociation (ν_{OH} , C–O–H bend, C–C–O–H torsion) were conserved. Although these vibrational energies are not conserved, the energetic requirement for the process if they were conserved provides a useful guide to understanding the energetics of the trajectories. ^cThe average time between the last successful tunneling event and dissociation, which is assumed to occur 50 steps after the O–H distance of the bond being broken becomes greater than 6 Å.

condition has total energy 4.94 eV, which is the sum of potential energy of the equilibrium geometry of the S_1 state (4.42 eV shown in Figure 1) and the vibrational energy of our initial conditions (0.52 eV). For interpretative purposes, we consider a model of the trajectories in which the vibrational energies of spectator modes (nondisappearing vibrational modes) are conserved. Excluding the initial vibrational energy (~0.21 eV) of the disappearing mode O–H stretching at stationary points MECI1 and SP along the photodissociation reaction path, the vibrational energy of the system reduces to 0.31 eV, and the total energies that would be required for this model trajectory to reach the two stationary points are at least 5.66 eV (potential energy 5.35 eV plus vibrational energy 0.31 eV) and 5.45 eV (potential energy 5.14 eV plus vibrational energy 0.31 eV), respectively. In the product region, three modes, namely, the O–H stretch, the C–O–H bending with initial vibrational energy of 0.001 eV, and the C–C–O–H torsion with initial vibration energy of 0.013 eV, disappear compared to the reactant region, and the vibrational energy further reduces to 0.30 eV. The energy of the ground-state products tied up in vibration in the model trajectory becomes 3.93 (potential energy) + 0.30 = 4.23 eV, and the first excited-state products have at least 4.74 + 0.30 = 5.04 eV. Similarly, we can obtain these energies for the other two ensembles. Because ensemble *b* differs from *a* only in the initial vibrational energy of the O–H mode, which is a disappearing mode for all the key stationary points (MECI1, SP, and products), all these stationary points except for those in the initial reactant region have the same energies listed as those of ensemble *a*. As we mentioned earlier in this section, some nondisappearing modes of ensemble *c* have more initial energies than in ensembles *a* and *b*, and this leads to a higher energy requirement for model trajectory *c* to reach the stationary points shown on the bottom of Figure 2.

Tunneling. The tunneling path is taken to be the O–H stretch internal coordinate by the method of refs 21 and 22. Note that none of the other internal coordinates are

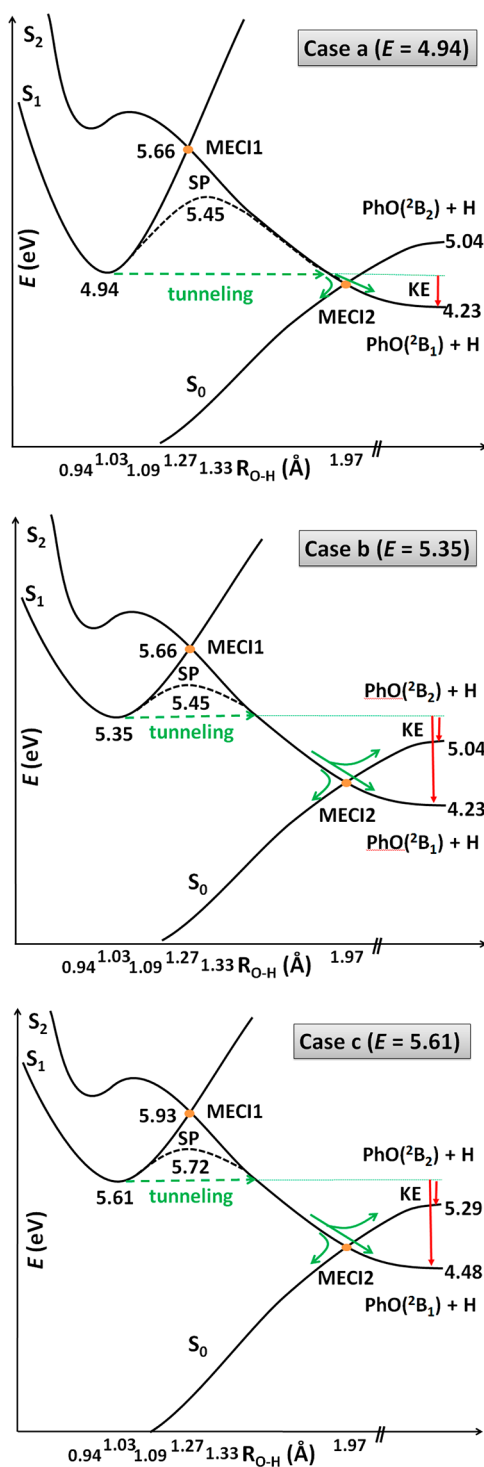


Figure 2. Schematic profiles of the model-trajectory energetics (see text) of the three ensembles along the photodissociation path of phenol. The differences between the total energy E and these product energies (red vertical arrows) are approximate upper limits on kinetic energy release. MECI denotes the minimum energy point on a conical intersection seam, and SP denotes the saddle point. The zero of energy is the minimum of S_0 state, which is not shown in the figure.

constrained to an equilibrium value, and each tunneling path has different values for the other 32 internal coordinates. Thus, the ensemble of tunneling paths samples a wide range of values of all 33 internal coordinates.

Termination Condition. Because the diabatic coupling in our fitted potential energy surfaces vanishes for O–H distances greater than 5 Å, except for the coupling due to the C–C–O–H torsion, which causes negligible coupling at such long distances, no further electronic transitions take place after 5 Å. A trajectory is terminated 50 integration steps after the O–H distance of the dissociating bond becomes 6 Å. In the complete mechanism, electronically excited phenoxyl produced by photodissociation can decay by unimolecular internal conversion after the H atom has departed (see, for example, the recent discussion of a similar process in pyrrole³²); we consider this to be a separate kinetic step, and it is not considered here. Note that the relative translational energy is independent of whether such postdissociative internal conversion occurs, so the calculated final relative translational energies are the same as if they were measured several cm away from the photoinduced process, as might be the case experimentally.

RESULTS

Figure 2 shows that none of the three ensembles has enough energy to pass through either MECI1 or SP without tunneling. However, we included multidimensional tunneling along the OH stretch coordinate by the method of ref 22. Table 1 shows the total number of trajectories we run for each ensemble, the number of reactive (dissociated) trajectories, and the number of reactive trajectories without tunneling. No trajectories react without tunneling for $E = 4.94$ eV. Only one out of 7631 and eight out of 10 362 reactive trajectories for $E = 5.35$ and 5.61 eV do not involve tunneling, which clearly confirms that hydrogen tunneling is the main reaction mechanism of phenol photodissociation and that the present study would not have been possible without the new tunneling method of ref 22.

The calculated lifetimes of the S_1 state for $E = 5.35$ and 5.61 eV, which correspond to one quantum excitation of ν_{OH} mode in S_1 state, are 0.88 and 0.66 ns, respectively, and are reasonably shorter than the experimental observation¹⁵ of ~ 2 ns for 0–0 excitation.

The distributions of the product kinetic energy are in Figure 3. The calculated maximum kinetic energies that would be observed if vibrational energies of nondissipating modes were conserved, as based on the energetics in Figure 2, are marked using purple and green vertical arrows, respectively, for excited and ground electronic-state products. Figure 3 shows that the histograms of the present simulations have similar shapes and trends as the experimental kinetic energy spectra.¹⁶ Recall that the simulations with initial conditions *a* correspond approximately to the experimental 0–0 excitation, and we note that the simulations with initial conditions *b* and *c* are more like the photodissociation experiments with $\lambda \sim 239$ –252 nm (see Supporting Information). As shown in Figure 2, case *a* has lower energy than the energy of excited-state products including vibration, so only ground-state products can be obtained if spectator-mode vibrational energy is conserved. However, the $\sim 4\%$ excited-state products are observed because the present semiclassical simulations do not completely retain vibrational energies of modes that persist in the products, whereas quantum simulations of the 0–0 photodissociation would conserve ZPE (this is a well-known deficiency of trajectory simulations³³). This may also be the reason that the slow kinetic energy peaks of our simulations for the two higher-energy cases center at slightly higher kinetic energy than those of experiments.

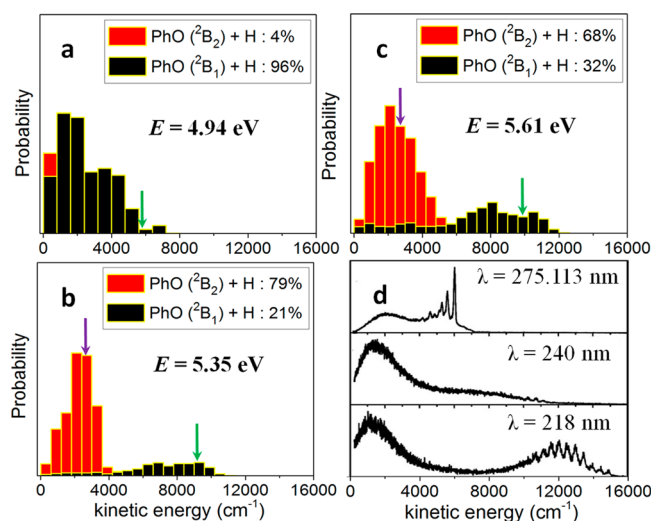


Figure 3. (a–c) Histograms of kinetic energy for cases *a*, *b*, and *c*. (d) Experimental¹⁶ kinetic energy spectra. The vertical arrows correspond to the vertically downward arrows in Figure 2 and are the maximum kinetic energies that would be observed if vibrational mode energies of nondissipating modes were conserved: purple and green, respectively, for excited and ground electronic-state products. Part d is reprinted with permission from ref 16. Copyright 2011, American Institute of Physics. The smallest wavelength (218 nm) in this figure is for a higher energy than is studied in this article and is shown only to illustrate the trend in the kinetic energy distribution as a function of excitation energy.

The slow kinetic energy component centered at ~ 2000 cm⁻¹ in the experiments under 0–0 excitation (275.113 nm) is due to the accumulation of vibrational energy in the ground-electronic-state products. As shown in Figure 2 and Table 1, in cases *b* and *c* the excitation of the ν_{OH} mode provides enough energy to produce electronically excited products after passing the second intersection region. The branching ratio of products is shown in Figure 3. As pointed out above, the trajectory simulations do not correspond precisely to the experimental initial conditions, but the experimental kinetic energy distributions are shown to illustrate the general trend in the excitation energy dependence of the kinetic energy release observed experimentally. The final-state analysis of the present simulations clearly shows that for the energies of simulations *b*

and *c*, the slow kinetic energy peak is mainly due to production of electronically excited products rather than ground-electronic-state products as postulated by Nix et al.⁸ (although, as discussed above, we are considering only the initial photodissociation and not any subsequent unimolecular internal conversion, whereas the experimental detection may actually occur after internal conversion has occurred), and the fast kinetic energy component is due to ground-electronic-state products. The present explanation for the slow kinetic energy release agrees with the observations of Hause et al.¹⁰ for the dissociation of phenol-*d*₅ with an initially excited O–H stretching vibration. The first excited-state products were also reported in King et al.'s work¹³ for $\lambda = 230$ nm and also Idbal et al.'s work¹⁴ for $\lambda = 200$ nm. In addition, we found a small proportion of the slow peak is from highly vibrationally excited ground-electronic-state products produced by direct dissociation. An important advantage of simulations over experiments is that in experiments performed to date the low vibrational states of the excited electronic state cannot be distinguished from the high vibrational states of the ground electronic state, whereas Figure 3 provides this separation.

The branching ratio of the products was also identified in some earlier 2-D time-dependent quantum wave packet dynamics studies of photodissociation of phenol.^{6,34} However, a 2-D simulation cannot model the vibrational energy release in a system with many degrees of freedom, and therefore cannot predict the final kinetic energy distribution.

Vibrational mode selectivity was inferred based on the vibrationally resolved high-kinetic-energy end of the kinetic energy spectrum.^{7,8,16} But product vibrational modes can be preferentially excited not only because systems with these modes excited in *S*₁ react preferentially, but also because the modes accept energy released after passing the highest potential energy on the dissociation path. The trajectory simulations do not yield quantized final vibrational energies, but we can draw mechanistic conclusions by comparing the change of vibrational energy of each mode from reactants to products, and by computing average values ($\langle n \rangle$), obtained with the harmonic-oscillator approximation³⁵) of the quantized unitless action variables that are classical analogues of vibrational quantum numbers. Table 2 lists the four in-plane and two out-of-plane modes where $\langle n \rangle$ increases the most: for in-plane, the CO stretch, ν_{CO} , C–C–C bending modes ν_{12} , and ν_{6a} , and in-plane

Table 2. Active Vibrational Modes^a

| <i>E</i> (eV) | mode | ν_{CO} | ν_{12} | ν_{6a} | ν_{18b} | ν_{16a} | ν_{11} |
|---------------|--|-------------------|----------------|------------|-------------|------------------|------------|
| | type | stretch | CCC bend modes | | CO wag | ring distortions | |
| | symmetry | a' | a' | a' | a' | a'' | a'' |
| <i>a</i> | initial E_{vib} | 8 | 8 | 8 | 8 | 105 | 105 |
| | final $\langle E_{\text{vib}} \rangle$ | 1051 | 389 | 275 | 266 | 278 | 172 |
| | change of $\langle n \rangle$ | 0.69 | 0.47 | 0.49 | 0.57 | 0.45 | 0.35 |
| <i>b</i> | initial E_{vib} | 8 | 8 | 8 | 8 | 105 | 105 |
| | final $\langle E_{\text{vib}} \rangle$ | 990 | 346 | 284 | 183 | 199 | 1207 |
| | change of $\langle n \rangle$ | 0.65 | 0.41 | 0.51 | 0.39 | 0.24 | 5.74 |
| <i>c</i> | initial E_{vib} | 105 | 105 | 105 | 105 | 105 | 105 |
| | final $\langle E_{\text{vib}} \rangle$ | 1059 | 781 | 266 | 217 | 291 | 141 |
| | change of $\langle n \rangle$ | 0.63 | 0.83 | 0.30 | 0.26 | 0.48 | 0.18 |

^aWe use Wilson's notation³⁶ for modes; energies are in cm⁻¹; $\langle E_{\text{vib}} \rangle$ and $\langle n \rangle$ are the average vibrational energy and quantum number for specific modes of ground-electronic-state phenoxyl products. This table lists the four a' modes with the largest increase in $\langle n \rangle$ and the two a'' modes with the largest increase in $\langle n \rangle$, where the classical vibrational action variable is $(n + 1/2)h$ and h is Planck's constant. Energies in modes (E_{vib}) are in cm⁻¹. Modes of a' symmetry are in-plane vibrations, and modes of a'' symmetry are out-of-plane vibrations.

CO wagging mode ν_{18b} , and for out-of-plane, the ring distortion modes ν_{16a} and ν_{11} . The latter two modes promote state couplings that (i) lower the adiabatic barrier and thereby promote tunneling and (ii) promote adiabatic behavior thereby decreasing diabatic recrossing back to phenol. It is encouraging that the modes ν_{16a} , ν_{11} , ν_{6a} and ν_{18b} were also observed to be excited in experiments.^{8,16} Excitation of ν_{CO} and ν_{12} can be explained by the fact that the equilibrium C–O distance decreases by 0.12 Å and the equilibrium C–C–C angles change by as much as -3° in progressing to 2B_1 phenoxyl.²⁰

An important aspect of the simulations is that they yield more information about the reaction path and mechanism than is available experimentally; for example, if we use V_1 , V_2 , and V_3 to label the three lowest adiabatic states and U_1 , U_2 , and U_3 to label the diabatic states ($^1\pi\pi^*$, $^1\pi\pi^*$, and $^1\pi\sigma^*$), the minimum of (V_3-V_2) along a trajectory will indicate how close the two adiabatic states are to each other, and the minimum of $|U_3-U_2|$ will show how close the diabatic states $^1\pi\pi^*$ and $^1\pi\sigma^*$ are to each other. We recall, as explained above, that in different regions of the global space the diabatic states can correspond to different adiabatic labels because of the state crossings and avoided crossings, and we must keep in mind that V_1 , V_2 , and V_3 are always ordered based on the adiabatic energy. Figure 4 plots the distributions of the minimum of (V_3-V_2) in the classical regions, i.e., excluding tunneling regions, and the (U_2-U_3) distribution at the minimum of $|U_3-U_2|$ (left column), and the distributions of (U_2-U_3) at the minimum of (V_3-V_2) for dissociated trajectories, and these plots show that most trajectories have a minimum value of (V_3-V_2) that is greater

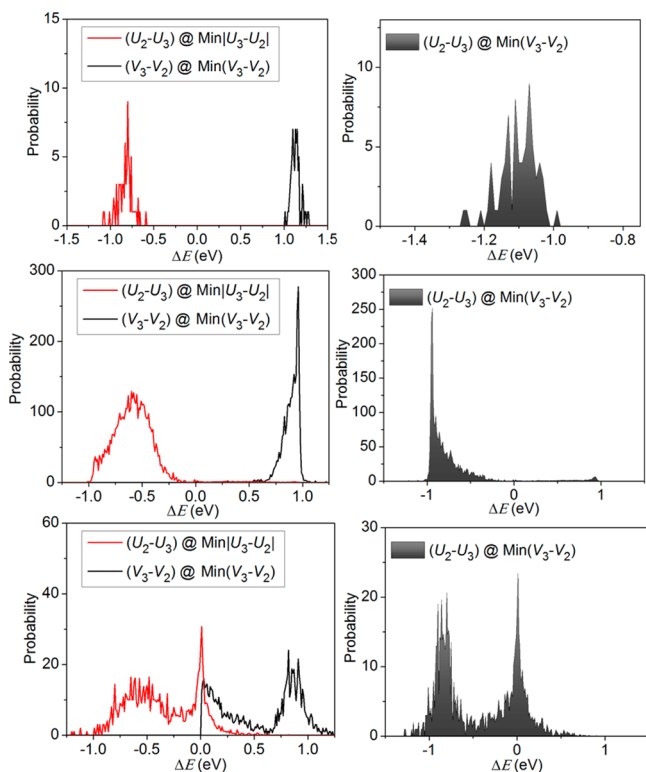


Figure 4. Distributions (in the classical regions, i.e., excluding tunneling regions) of (V_3-V_2) at the minimum of (V_3-V_2) and the (U_2-U_3) distribution at the minimum of $|U_3-U_2|$ (left column), and the distributions of (U_2-U_3) at the minimum of (V_3-V_2) for dissociated trajectories. Top, $E = 4.94$ eV; middle, $E = 5.35$ eV; bottom, $E = 5.61$ eV.

than 0.6 eV for all the three ensembles, but some of trajectories of ensemble c pass very close to the conical intersection of the $^1\pi\pi^*$ and $^1\pi\sigma^*$ states.

The left column of Figure 5 shows the R_{OH} distributions at starting points, points of maximum V_{eff} (that is, of maximum

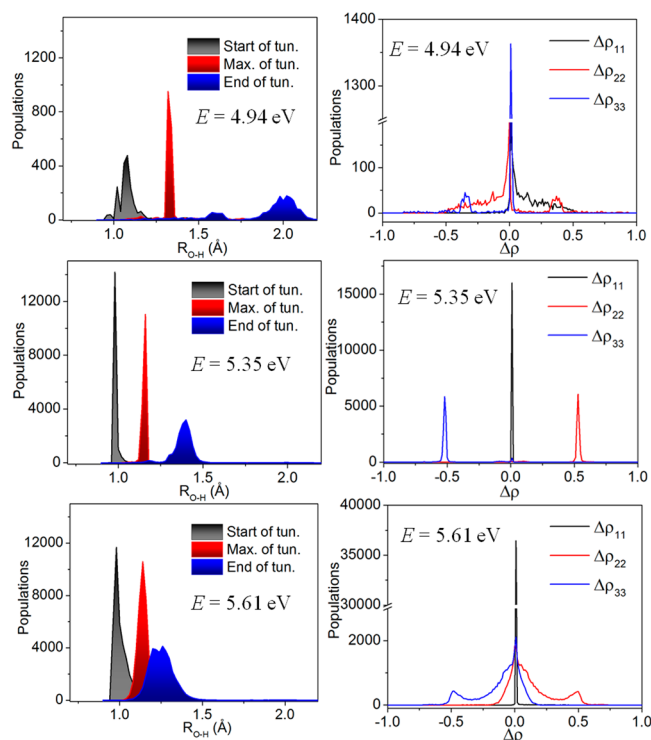


Figure 5. R_{OH} distribution at three points during the tunneling events, and the adiabatic state population changes ($\Delta\rho_{ij}$) during tunneling.

SCP), and ending points of the successful tunneling paths, and the right column plots the distributions of the changes in the populations (as measured by the changes $\Delta\rho_{ij}$ in diagonal elements of the adiabatic electronic density matrix) that occur during the tunneling events. The two higher-energy ensembles, in which the O–H stretch mode is initially excited, usually start their tunneling at short R_{OH} (~ 0.9 – 1.0 Å). The system is initially in the bound S_1 state (whose adiabatic and diabatic ($^1\pi\pi^*$) potentials are called V_2 and U_2 at small R_{OH}), but reaction leads to the either the $^1\pi\pi$ state (V_2 or U_1 at large R_{OH}) or the $^1\pi\sigma^*$ state (V_1 or U_3 at large R_{OH}). As shown in Figure 1, in the region of $R_{OH} \sim 0.9$ Å, the S_2 state PES (V_3 or U_3 at small R_{OH}) has a shallow well, where evolution of the electronic wave function along a trajectory can introduce a large coherent weight (up to $\sim 75\%$ for $E = 5.35$ eV, up to $\sim 90\%$ for $E = 5.61$ eV) of the U_3 state in the SCP. Figure 6 shows representative trajectories. For the two higher-energy cases, the tunneling events all start in that small R_{OH} region with a relatively high weight of V_3 (which is U_3 in that region) in the V_{eff} and then they tunnel through the avoided crossing of V_2 and V_3 and end in a region where U_3 is lower than U_2 or nearly degenerate with it. The right side of Figure 5 shows that evolution of wave functions along tunneling paths leads to an increase of population of U_3 (which is usually V_2 at the end of the tunneling event, so that this corresponds to positive $\Delta\rho_{22}$ in the adiabatic representation) and a decrease of the weight of U_2 (usually V_3 at the end of tunneling, hence negative $\Delta\rho_{33}$). This mechanism, involving tunneling in a coherent mixture of states

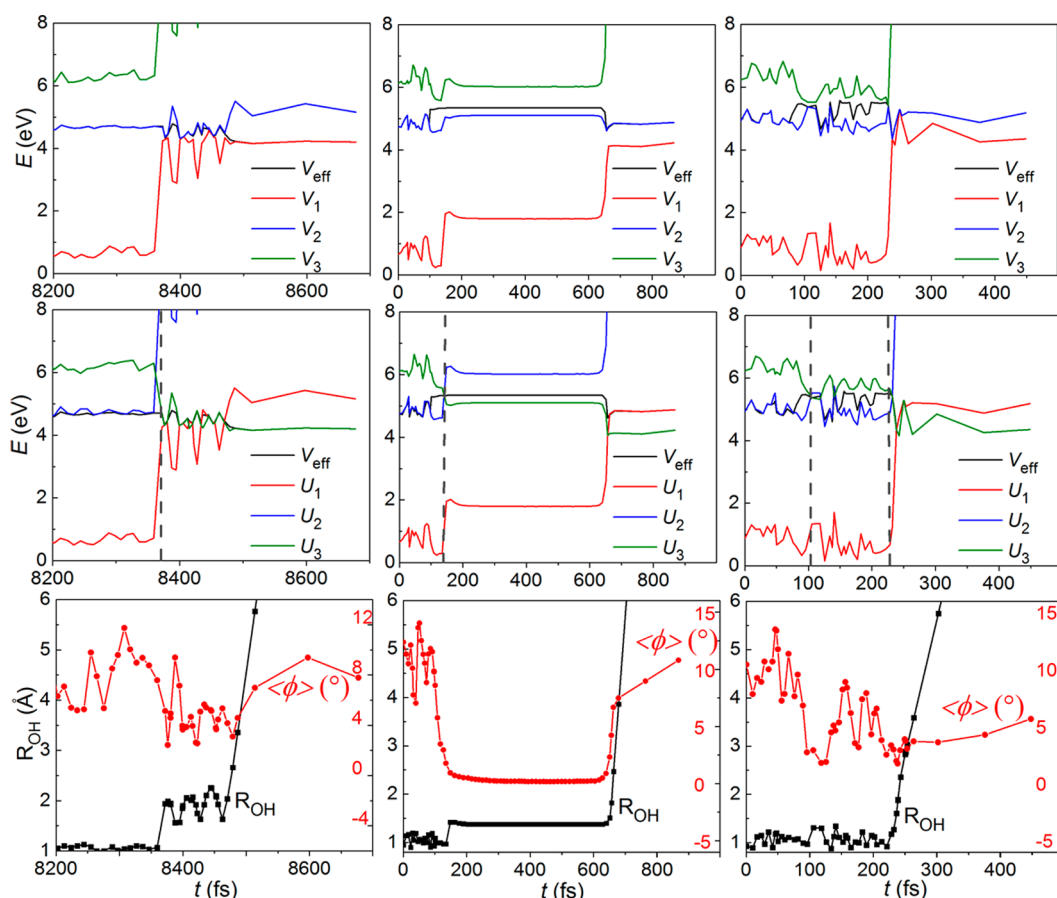


Figure 6. Representative trajectories for $E =$ (left) 4.94, (middle) 5.35, and (right) 5.61 eV in classical region. The vertical dashed lines mark the places where tunneling events happen; V_{eff} is the SCP; $\langle\phi\rangle$ is the average of 10 nonredundant out-of-plane angles.

in the smaller R_{OH} region, was quite unexpected since previous discussion of tunneling has all focused on the adiabatic SP at larger R_{OH} .

For $E = 5.61$ eV, some tunneling ends on the U_3 potential near the U_3/U_2 crossing, but before the V_3/V_2 crossing (CI1), that is, U_3 is still V_3 at the end of the tunneling event, thus a small number of trajectories with negative $\Delta\rho_{22}$ and positive $\Delta\rho_{33}$ are seen in Figure 5. More than one tunneling event can occur before the dissociation. Without tunneling, the system can be trapped in the inner well without dissociation or has to decrease the U_3 weight in the V_{eff} to stay mainly on the U_2 state.

At $E = 4.94$ eV, there is not enough energy to introduce a large weight of the U_3 state, so that this ensemble has to tunnel through a longer path (~ 1 Å of R_{OH} increase) compared to the other two ensembles. It also takes longer times (>8 ps in the representative trajectory shown in Figure 6) to begin to tunnel, so the rate is lower. During the long-path tunneling, the system involves some coherent population of the ground state that lowers V_{eff} ; this results in the positive $\Delta\rho_{11}$ observed in the right top of Figure 5. At the end of the long-path tunneling, U_3 (which is V_3 at the start of the tunneling event) becomes V_2 ; thus, those paths involving small weight of U_3 at the start of tunneling are responsible for the negative $\Delta\rho_{33}$ and positive $\Delta\rho_{22}$ peaks. At the end of tunneling, the electronic populations ρ_{11} and ρ_{22} are distributed in the ranges 0–0.5 and 0.5–1.0 (for more data on population, the reader is referred to Figure S5 in Supporting Information); this indicates that the reaction following 0–0 excitation is mainly caused by direct dissociation instead of indirect dissociation via internal conversion.

After successful tunneling the systems need some time to adjust the populations on the three states to find a path with a suitable V_{eff} to cause dissociation. Table 1 lists the average times; a longer average time (0.9 ps; Table 1) is found for $E = 5.35$ eV, because, in order to introduce a larger weight of U_3 at the start of tunneling, it converts most of the energy into potential energy, and the low kinetic energy slows down the process. This shows up as almost unchanged potentials and geometries for a time range of ~ 0.5 ps in the trajectory for $E = 5.35$ eV in Figure 6, which is not untypical.

The longer tunneling paths at $E = 4.94$ eV tend to lead the system directly to the vicinity of CI2, and most of the dissociated trajectories directly pass through the CI2 region to ground-electronic-state products. Plotting the distributions of minimum of $V_2 - V_1$ in the dissociated trajectories (Figure 7) shows that ensembles *b* and *c* tend to dissociate adiabatically to excited-state products by passing through the avoided crossing of V_2/V_1 near CI2. The geometries at the minima of $V_2 - V_1$ of the three ensembles all deviate slightly from the planar structures, and the averages of the 10 out-of-plane non-redundant angles²⁰ are mainly distributed in the region of 8–22° (see Figure S3 in Supporting Information). This shows the importance of understanding nonplanar conical intersections, which have been relatively unappreciated.³⁷

SUMMARY

The present multistate CSDM trajectory simulations including tunneling, based on full-dimensional APRP potentials and state couplings, agree with experiment for the bimodal nature of the

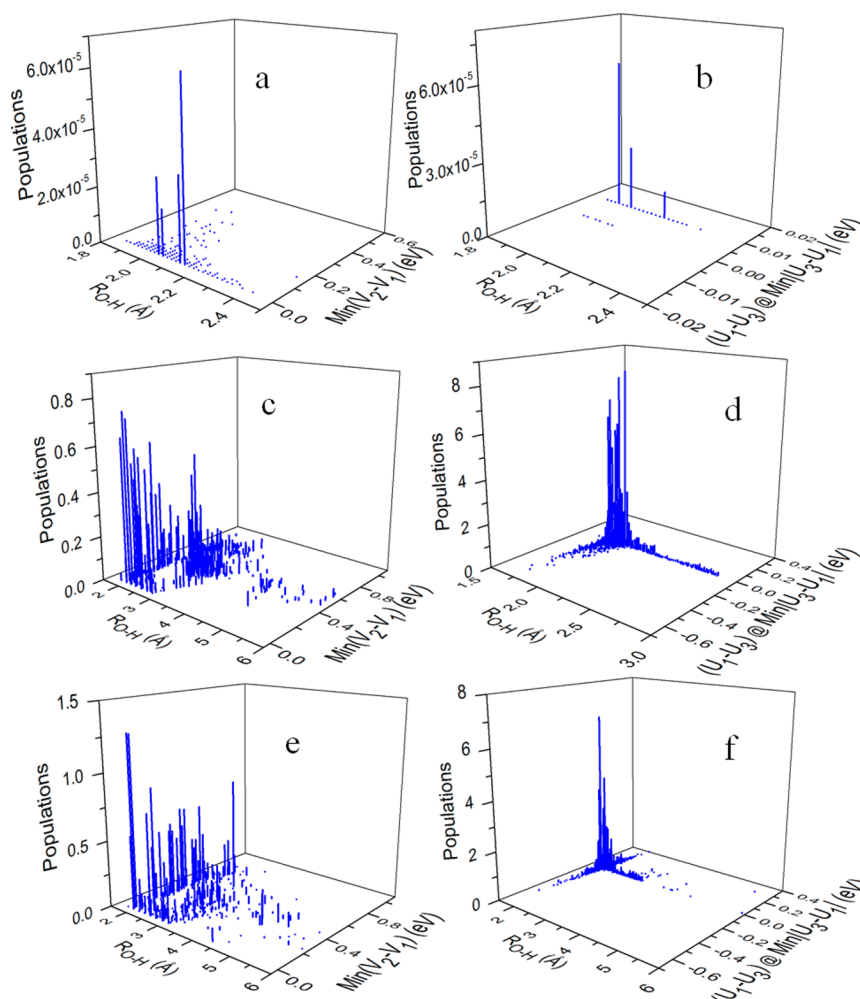


Figure 7. 3D distributions in the classical region of the minimum of $(V_2 - V_1)$ and the corresponding R_{OH} distance (a, c, and e) and the $(U_1 - U_3)$ distribution at the minimum of $|U_3 - U_1|$ and the corresponding R_{OH} distance (b, d, and f) of each dissociated trajectory. (a,b) $E = 4.94$ eV; (c,d) $E = 5.35$ eV; (d,e) $E = 5.61$ eV.

kinetic energy spectra for the photodissociation of phenol, and they provide direct evidence that the low kinetic energy release is not because of indirect statistical decay but mainly due to direct dissociation to ground- (for the low-energy case) and excited- (for cases with initially excited OH stretching mode) electronic-state products, and show the important role of the coherence of electronic states in dynamics. The details of dynamics that cannot be obtained experimentally and by theoretical simulations only considering two or three important coordinates are uncovered by statistical analysis made possible by running a large number of full-dimensional dissociating trajectories, where the dissociation is enabled by tunneling.

■ ASSOCIATED CONTENT

■ Supporting Information

More statistical analysis of the simulations. This material is available free of charge via the Internet at <http://pubs.acs.org>.

■ AUTHOR INFORMATION

Corresponding Author

truhlar@umn.edu

Notes

The authors declare no competing financial interest.

■ ACKNOWLEDGMENTS

The authors appreciate helpful discussions with Michael Ashfold. This work was supported in part by U.S. Department of Energy, Office of Basic Energy Sciences, under SciDAC Grant No. DE-SC0008666.

■ REFERENCES

- (1) Sobolewski, A. L.; Domcke, W.; Dedonder-Lardeux, C.; Jouvet, C. *Phys. Chem. Chem. Phys.* **2002**, *4*, 1093–1100.
- (2) Crespo-Hernández, C. E.; Cohen, B.; Hare, P. M.; Kohler, B. *Chem. Rev.* **2004**, *104*, 1977–2019.
- (3) Roberts, G. M.; Hadden, D. J.; Bergendahl, L. T.; Wenge, A. M.; Harris, S. J.; Karsili, T. N. V.; Ashfold, M. N. R.; Paterson, M. J.; Stavros, V. G. *Chem. Sci.* **2013**, *4*, 993–1001.
- (4) Schick, C. P.; Weber, P. M. *J. Phys. Chem. A* **2001**, *105*, 3725–3734.
- (5) Tseng, C. M.; Lee, Y. T.; Ni, C. K. *J. Chem. Phys.* **2004**, *121*, 2459–2461.
- (6) Lan, Z.; Domcke, W.; Vallet, V.; Sobolewski, A. L.; Mahapatra, S. *J. Chem. Phys.* **2005**, *122*, 224315.
- (7) Ashfold, M. N. R.; Cronin, B.; Devine, A. L.; Dixon, R. N.; Nix, M. G. D. *Science* **2006**, *312*, 1637–1640.
- (8) Nix, M. G. D.; Devine, A. L.; Cronin, B.; Dixon, R. N.; Ashfold, M. N. R. *J. Chem. Phys.* **2006**, *125*, 133318.
- (9) Tseng, C. M.; Lee, Y. T.; Lin, M. F.; Ni, C. K.; Liu, S. Y.; Lee, Y. P.; Xu, Z. F.; Lin, M. C. *J. Phys. Chem. A* **2007**, *111*, 9463–9470.

- (10) Hause, M. L.; Yoon, Y. H.; Case, A. S.; Crim, F. F. *J. Chem. Phys.* **2008**, *128*, 104307.
- (11) Ashfold, M. N. R.; Devine, A. L.; Dixon, R. N.; King, G. A.; Nix, M. G. D.; Oliver, T. A. A. *Proc. Natl. Acad. Sci. U.S.A.* **2008**, *105*, 12701–12706.
- (12) Nix, M. G. D.; Devine, A. L.; Dixon, R. N.; Ashfold, M. N. R. *Chem. Phys. Lett.* **2008**, *463*, 305–308.
- (13) King, G. A.; Oliver, T. A. A.; Nix, M. G. D.; Ashfold, M. N. R. *J. Phys. Chem. A* **2009**, *113*, 7984–7993.
- (14) Idbal, A.; Cheung, M. S. Y.; Nix, M. G. D.; Stavros, V. G. *J. Phys. Chem. A* **2009**, *113*, 8157–8163.
- (15) Pino, G. A.; Oldani, A. N.; Marceca, E.; Fujii, M.; Ishiuchi, S.-I.; Miyazaki, M.; Broquier, M.; Dedonder, C.; Jouvét, C. *J. Chem. Phys.* **2010**, *133*, 124313.
- (16) Dixon, R. N.; Oliver, T. A. A.; Ashfold, M. N. R. *J. Chem. Phys.* **2011**, *134*, 194303.
- (17) Roberts, G. M.; Chatterley, A. S.; Young, J. D.; Stavros, V. G. *J. Phys. Chem. Lett.* **2012**, *3*, 348–352.
- (18) (a) Zhang, Y.; Oliver, T. A. A.; Ashfold, M. N. R.; Bradforth, S. E. *Faraday Discuss.* **2012**, *157*, 141–163. (b) Karsili, T. N. V.; Wenge, A. M.; Marchetti, B.; Ashfold, M. N. R. *Phys. Chem. Chem. Phys.* **2014**, *16*, 588–598.
- (19) Xu, X.; Yang, K. R.; Truhlar, D. G. *J. Chem. Theory Comput.* **2013**, *9*, 3612–3625.
- (20) Yang, K. R.; Xu, X.; Zheng, J.; Truhlar, D. G. *Chem. Sci.* **2014**, *5*, 4661–4680.
- (21) Zheng, J.; Xu, X.; Meana-Pañeda, R.; Truhlar, D. G. *Chem. Sci.* **2014**, *5*, 2091–2099.
- (22) Zheng, J.; Meana-Pañeda, R.; Truhlar, D. G. *J. Phys. Chem. Lett.* **2014**, *5*, 2039–2043.
- (23) (a) Zhu, C.; Nangia, S.; Jasper, A. W.; Truhlar, D. G. *J. Chem. Phys.* **2004**, *121*, 7658–7670. (b) Jasper, A. W.; Zhu, C.; Nangia, S.; Truhlar, D. G. *Faraday Discuss.* **2004**, *127*, 1–22. (c) Jasper, A.; Truhlar, D. G. In *Conical Intersections: Theory, Computation, and Experiment*; Domcke, W.; Yarkony, D. R.; Köppel, H., Eds.; Advanced Series in Physical Chemistry 17; World Scientific: Singapore, 2011; pp 375–414.
- (24) Yang, K. R.; Xu, X.; Truhlar, D. G. *J. Chem. Theory Comput.* **2014**, *10*, 924–933.
- (25) (a) Nakano, H. *J. Chem. Phys.* **1993**, *99*, 7983–7992. (b) Nakano, H. *Chem. Phys. Lett.* **1993**, *207*, 372–378.
- (26) Papajak, E.; Truhlar, D. G. *J. Chem. Theory Comput.* **2010**, *6*, 597–601.
- (27) Kendrick, B. K.; Mead, C. A.; Truhlar, D. G. *Chem. Phys.* **2002**, *277*, 31–41.
- (28) (a) Nakamura, H.; Truhlar, D. G. *J. Chem. Phys.* **2002**, *117*, 5576–5593. (b) Yang, K. R.; Xu, X.; Truhlar, D. G. *Chem. Phys. Lett.* **2013**, *573*, 84–89.
- (29) Bohm, A. *Quantum Mechanics: Foundations and Applications*; 3rd ed.; Springer-Verlag: New York, 1993; p 64.
- (30) Truhlar, D. G.; Mucjerman, J. T. In *Atom-Molecule Collision Theory: A Guide for the Experimentalist*; Bernstein, R. B., Ed.; Plenum: New York, 1979; pp 505–566.
- (31) Ryckaert, J. P.; Cicotti, G.; Berendsen, H. J. C. *J. Comput. Phys.* **1977**, *23*, 327–341.
- (32) Saita, K.; Nix, M. G. D.; Shalashilin, D. V. *Phys. Chem. Chem. Phys.* **2013**, *15*, 16227–16235.
- (33) (a) Gray, J. C.; Truhlar, D. G.; Clemens, L.; Duff, J. W.; Chapman, F. M., Jr.; Morrell, G. O.; Hayes, E. F. *J. Chem. Phys.* **1978**, *69*, 240–252. (b) Bonhommeau, D.; Truhlar, D. G. *J. Chem. Phys.* **2008**, *129*, 14302.
- (34) An, H.; Baeck, K. K. *J. Phys. Chem. A* **2011**, *115*, 13309–13315.
- (35) Corchado, J. C.; Espinosa-Garcia, J. *Phys. Chem. Chem. Phys.* **2009**, *11*, 10157–10164.
- (36) Wilson, E. B. *Phys. Rev.* **1934**, *45*, 706–714.
- (37) Harris, S. J.; Murdock, D.; Zhang, Y.; Oliver, T. A. A.; Grubb, M. P.; Orr-Ewing, A. J.; Greetham, G. M.; Clark, I. P.; Towrie, M.; Bradforth, S. E.; Ashfold, M. N. R. *Phys. Chem. Chem. Phys.* **2013**, *15*, 6567–6582.